



Cobalt phosphide with porous multishelled hollow structure design realizing promoted ammonia borane dehydrogenation: Elucidating roles of architectural and electronic effect

Ping Li ^{a,b,*}, Yuqi Huang ^{a,b}, Quhua Huang ^{a,b}, Ran Chen ^{a,b}, Jixin Li ^{a,b}, Shuanghong Tian ^{a,b}

^a School of Environmental Science and Engineering, Sun Yat-sen University, Guangzhou, 510275 Guangdong, PR China

^b Guangdong Provincial Key Laboratory of Environmental Pollution Control and Remediation Technology, Guangzhou 510275, PR China

ARTICLE INFO

Keywords:

Transition metal phosphide
Multishelled hollow structure
Electronic effect
d-band center
Ammonia borane dehydrogenation

ABSTRACT

Exploring advanced non-noble metal-based catalysts for H₂ release from chemical hydrogen storage materials is of paramount importance to boost hydrogen economy. Rationally tailoring over architecture and electronic state promises high-efficiency catalysis. Herein we present, for the first time, delicate engineer of cobalt phosphide with a unique porous, multishelled, and hollow architecture (multishelled Co-P) for dramatically promoting ammonia borane (AB) dehydrogenation. Featuring hollow porous structure and complex nanoconfined interior space, multishelled Co-P possesses abundant accessible active sites and facile mass transfer. Importantly, theoretical calculations decipher that P incorporation in Co-P can modulate electronic structure of Co sites to give promoted H₂O adsorption and favorable H₂O dissociation kinetics (rate-determining step), thereby facilitating AB dehydrogenation. This study provides a fundamental understanding of correlation between electronic state of Co-P and AB dehydrogenation behavior, and highlights that decent architectural engineering coupled with electronic modulation is an effective protocol to construct advanced catalytic systems.

1. Introduction

Hydrogen evolution via catalytic dehydrogenation of the chemical hydrogen storage materials is regarded as an effective and appealing route to boost future hydrogen paradigm [1,2]. Ammonia borane (NH₃BH₃, AB), with commendable air stability and high hydrogen content (19.6 wt%), is one of competitive hydrogen storage chemicals for portable applications [3–5]. Noble metals (such as Pt, Rh, and Ru) are identified as the state-of-the-art catalysts for AB dehydrogenation, yet their high cost and rarity hinder their large-scale implementations [6–8]. In this regard, to enable practical applications of AB as hydrogen carrier, developing cost-effective and earth-abundant catalysts as alternatives to precious metals is highly imperative [5,6,9].

In recent years, a variety of economical non-noble transition metal-based materials [6,9], including zero-valent transition metals [10–12], alloys [13,14], oxides [15–17], and borides [18], have been investigated to expedite dehydrogenation of AB. Among them, transition metal phosphides (TMPs), with unique electronic structure and satisfactory stability, have emerged as a class of promising candidates for catalytic AB dehydrogenation [19–23]. Unfortunately, the current TMPs still

show limited catalytic behavior, underperforming the state-of-the-art noble metal counterparts. The main reason lies in the undesirable mass transfer and insufficient catalytic centers due to the underdeveloped structural architectures. Besides, studies on the correlation between the electronic state of TMPs and catalytic AB hydrolysis property remains elusive, and the underlying promoted mechanism of TMPs is still not well understood, seriously hindering the reasonable engineering of advanced TMP-based catalysts for AB dehydrogenation.

On the other hand, it has been widely acknowledged that the morphological architecture has a significant impact on the performance of the catalyst material [24–26]. A rational and well-developed textural design would be conducive to full exposure of the active centers and smooth mass transfer as well [27,28]. Typically, hollow structure with porous multishells has gained an increasing amount of research interest during the past few years, due to large surface area, special interior space, abundant pores, and hierarchical architecture [29–32]. The above superior features make porous multishelled hollow structure serve as a class of promising candidate for versatile applications, such as catalysis, water treatment, sensor, and biomedicine [33–36]. On the basis of the above considerations, substantially enhanced catalytic

* Corresponding author at: School of Environmental Science and Engineering, Sun Yat-sen University, Guangzhou, 510275 Guangdong, PR China.

E-mail address: liping56@mail.sysu.edu.cn (P. Li).

<https://doi.org/10.1016/j.apcatb.2022.121444>

Received 23 March 2022; Received in revised form 20 April 2022; Accepted 22 April 2022

Available online 26 April 2022

0926-3373/© 2022 Elsevier B.V. All rights reserved.

property for AB hydrolysis can be expected via delicately fabricating the TMP with desirable porous multishelled hollow structure. However, to the best of our knowledge, no such investigation has been reported so far, thus motivating a detailed exploration.

In this work, we report, for the first time, a novel and effective synthetic approach to TMP with porous multishelled hollow structure for promoting hydrogen production from AB hydrolysis, using cobalt phosphide as the model material (hereafter denoted as multishelled Co-P for simplicity). Briefly, Co-containing metal-organic complex precursor (Co-MOC) was firstly prepared with a solvothermal method, then multishelled Co-P was derived from the precursor through a simple self-templating route followed by phosphidation. The as-obtained multishelled Co-P, featuring multiple shells, hollow porous structure, and unique interior space, could possess high exposure of plentiful accessible active sites, smooth mass transportation, and decent stability as well. As a result, the multishelled Co-P presents remarkable catalytic AB dehydrogenation performance, ranking one of the most active earth-abundant catalysts reported thus far. Impressively, systematical theoretical calculations reveal that P species incorporation in CoP can subtly modulate the electronic structure of the Co centers with upshift of the d-band center, giving rise to strengthened H₂O adsorption and follow-up promoted H₂O dissociation, thereby substantially accelerating AB dehydrogenation.

2. Experimental section

2.1. Preparation of the multishelled Co-P

In a typical synthesis, 1.5 mmol of Co(NO₃)₂·6H₂O, 0.15 g of trimesic acid (H₃BTC), and 1.0 g of polyvinylpyrrolidone (PVP) were dissolved in 30 mL of N,N-dimethylformamide (DMF). The resulting solution was transferred to a Teflon-lined stainless steel autoclave, and then heated at 433 K for 12 h. The purple-coloured powder product, Co-MOC, was collected after centrifugation, washing, and drying at 343 K overnight.

In the second step, the as-obtained Co-MOC was calcined at 673 K for 2 h under air atmosphere, thus yielding the multishelled Co₃O₄. Finally, the multishelled Co-P was obtained via facile phosphidation treatment of the multishelled Co₃O₄. In detail, the multishelled Co₃O₄ and a certain amount of NaH₂PO₂·H₂O (mass ratio = 1:20) were transferred to a tube furnace with NaH₂PO₂·H₂O at the upstream point. Then the furnace was heated to 573 K with a heating rate of 2 K/min, and kept at 573 K for 1 h under N₂ flowing. The black-coloured product, multishelled Co-P, was thus harvested.

2.2. Preparation of the control samples

The multishelled Co. The multishelled Co was fabricated by thermal reduction of the multishelled Co₃O₄ under H₂ atmosphere at 673 K for 2 h (heating rate = 2 K/min).

The solid Co-P. The solid Co-P was synthesized via the direct thermal phosphidation treatment of the Co-MOC precursor, and the phosphidation procedure was the same as that for the multishelled Co-P.

The comm Co-P. The comm Co-P was synthesized via the direct thermal phosphidation treatment of Co(NO₃)₂·6H₂O, and the phosphidation procedure was the same as that for the multishelled Co-P.

2.3. Catalytic performance investigation

The catalytic activity measurement was performed in a 50 mL two-necked round-bottom flask, with a constant temperature bath to maintain the temperature (298 K). A certain amount of catalyst and 3 mL of deionized water were first placed in the flask, then 1 mL of AB aqueous solution was injected by a syringe quickly to start the reaction. The volume of the evolved H₂ was monitored in real time by a water-filled gas burette with an accuracy of 0.5 mL. The TOF value was obtained according to the Eq. (1). To investigate the reaction activation energy

(E_a), hydrolytic dehydrogenation experiment was also performed at 303, 308, and 313 K. The E_a was obtained according to the Eq. (2). To perform the cycling test, the supernatant solution was removed and the catalyst was recollected via centrifugation and re-dispersed in deionized water, then AB aqueous solution was injected to start the next cycle of AB hydrolytic dehydrogenation.

$$\text{TOF} = \frac{V(\text{H}_2)/24.5}{n(\text{cat} - \text{TM}) * t(\text{min})} \quad (1)$$

$$\ln k = \ln A - E_a/RT \quad (2)$$

(k is the reaction rate, A is the pre-exponential factor, R is the gas constant, and T is the temperature.).

3. Results and discussion

3.1. Material synthesis and characterizations

The typical preparation protocol for the multishelled Co-P is illustrated in Scheme 1 and detailed in the Experimental Section. Co-containing metal-organic complex precursor (Co-MOC) was firstly prepared via a one-pot solvothermal method followed by air calcination to yield the multishelled Co₃O₄ hollow nanospheres. Then multishelled Co-P was derived via further phosphidation treatment of the multishelled Co₃O₄.

From the SEM and TEM images (Fig. 1a-c), the Co-MOC precursor possesses a solid nanospherical morphology (ca. 500–900 nm in particle size) with a smooth surface. The XRD pattern of the Co-MOC in Fig. 2a shows a weak diffraction peak at around 10°, which is consistent with those of TM-BTC MOF materials reported previously.[37,38] And the FTIR spectrum (Fig. 2b) further verifies the coordination of the Co species with the organic linker BTC [39]. Then based on the TGA result (Fig. 2c), the Co-MOC precursor was subjected to a facile calcination at 673 K under an air atmosphere to yield the multishelled Co₃O₄. The XRD pattern (Fig. 2a) of the calcination product shows the diffraction peaks readily indexed to the spinel phase of Co₃O₄ (PDF card no. 42–1467). From the FTIR spectrum (Fig. 2b), the disappearance of the peaks indexed to the organic ligands and the emergence of the absorption peaks at about 660 cm⁻¹ and 545 cm⁻¹ ascribed to stretching vibrations of the Co-O bonds together evidence the complete thermal decomposition of the Co-MOC and generation of Co₃O₄ [40]. The SEM and TEM images in Fig. 1d-f show that the calcination product largely inherits the original nanospherical morphology of the Co-MOC. Intriguingly, it presents a unique multishelled hollow structure with crumpled and rough shells, and the shells are porous and composed of a large number of interconnected nanoparticles (NPs, 10–15 nm in particle size). Herein, the formation of multishelled Co₃O₄ hollow structure can be ascribed to the occurrence of heterogeneous contraction induced by non-equilibrium heat treatment of the solid nanospheres of Co-MOC precursor. To be specific, with the combined effects of the contraction force caused by oxygenolysis and the adhesion force from the preformed outer Co₃O₄ shell during calcination, repeated interlaminar detachments would occur, ultimately resulting to unique multishelled hollow structure. Similar structural growth mechanism has been also adopted by several previously reported multishelled architectures [41, 42].

Through the reaction of the multishelled Co₃O₄ with PH₃ released from NaH₂PO₂·H₂O thermal decomposition, the multishelled Co-P can be achieved. As reported the XRD pattern of the phosphidated product in Fig. 2a, the emerged peaks can be well indexed to the orthorhombic phase of CoP (PDF card no. 29–0497), while the original peaks attributed to the spinel Co₃O₄ phase are no longer identified, signifying chemical transformation of the Co₃O₄ to CoP after the phosphidation process. In the FTIR spectrum of the multishelled Co-P (Fig. 2b), the wide band at around 1015 cm⁻¹ can be attributed to the bending vibration of

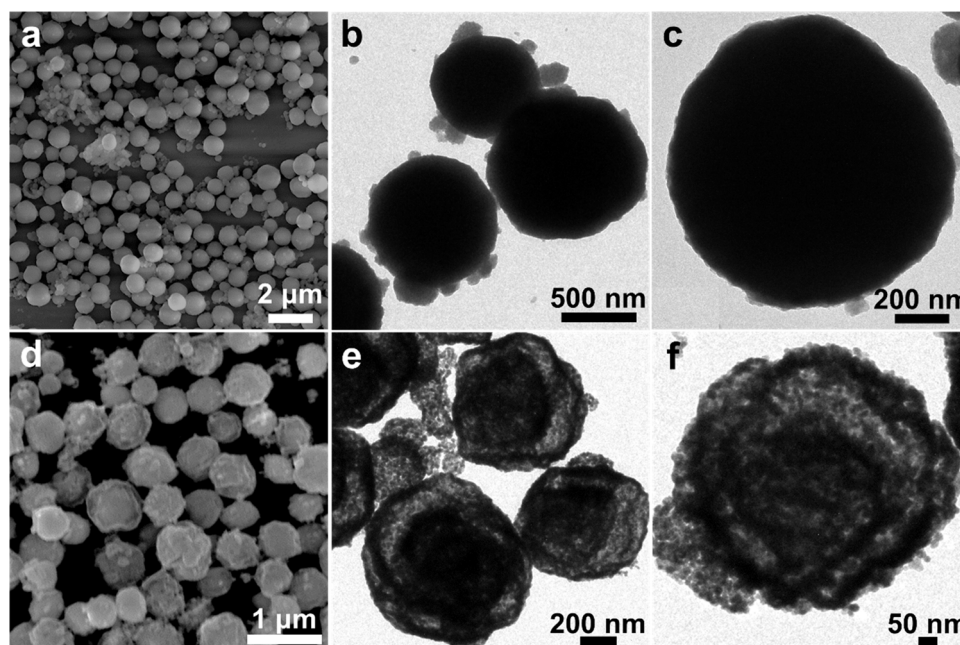
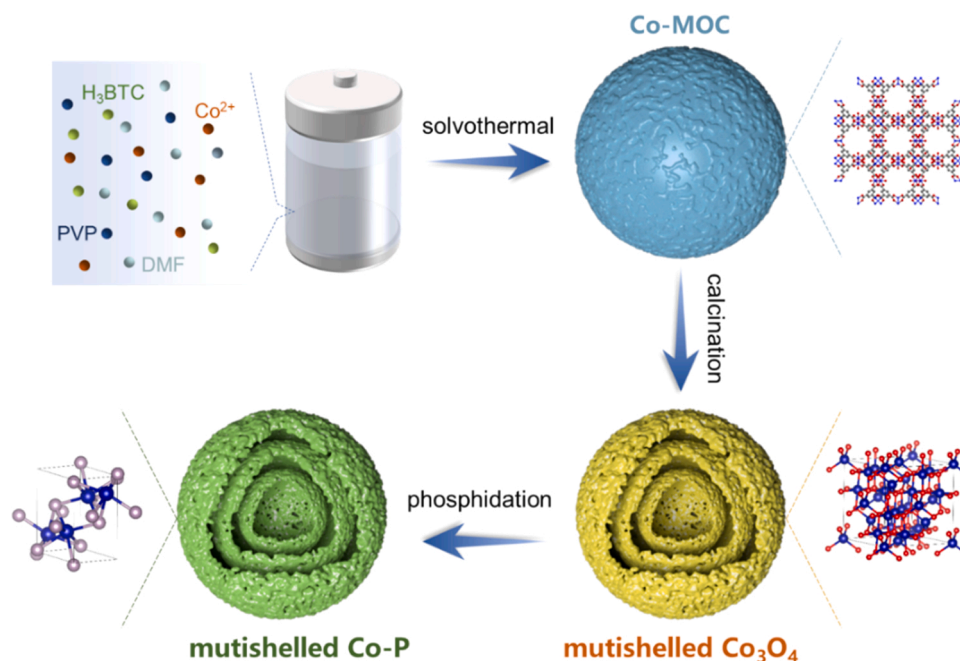


Fig. 1. (a) SEM and (b,c) TEM images of the Co-MOC precursor. (d) SEM and (e,f) TEM images of the multishelled Co_3O_4 .

Co-P bond, substantiating the formation of Co-P species [43]. From the SEM and TEM images in varied magnifications (Fig. 3a-d), the phosphidated product generally preserves the morphology of the multishelled Co_3O_4 , exhibiting similar porous multishelled hollow structure with building blocks of interconnected NPs in the range of 12–20 nm in size. The HRTEM image of the multishelled Co-P in Fig. 3e displays distinct lattice fringes with interplanar distances of 0.28 nm, consistent with the (011) planes of the orthorhombic phase of CoP. Moreover, the EDX elemental mappings in Fig. 3f reveal the homogeneous spatial distribution of Co and P elements within the whole multishelled Co-P spheres.

In addition, the textural property of the multishelled Co-P was characterized by nitrogen adsorption-desorption measurement. As depicted in Fig. S1a, the adsorption-desorption isotherm is type IV along

with an H3 type hysteresis loop ($P/P_0 > 0.7$), signifying the existence of mesoporous structure in slit-shape. And according to the NLDFT pore size distribution curve (Fig. S1b), the multishelled Co-P features a wide pore size distribution. The BET specific surface area is determined to be $25.1 \text{ m}^2/\text{g}$ and the total pore volume is $0.11 \text{ cm}^3/\text{g}$. Apparently, such special porous, multishelled, and hollow structure of Co-P is highly desirable for maximizing exposure of the active sites and smoothing mass diffusion, endowing the multishelled Co-P with enormous promise for high-performance catalysis. By contrast, the solid Co-P control possesses BET specific surface area of $0.9 \text{ m}^2/\text{g}$ and total pore volume of $0.003 \text{ cm}^3/\text{g}$ (Fig. S2a), obviously much smaller in comparison with those of the multishelled Co-P, resulting in deficient exposure of the active sites for catalysis.

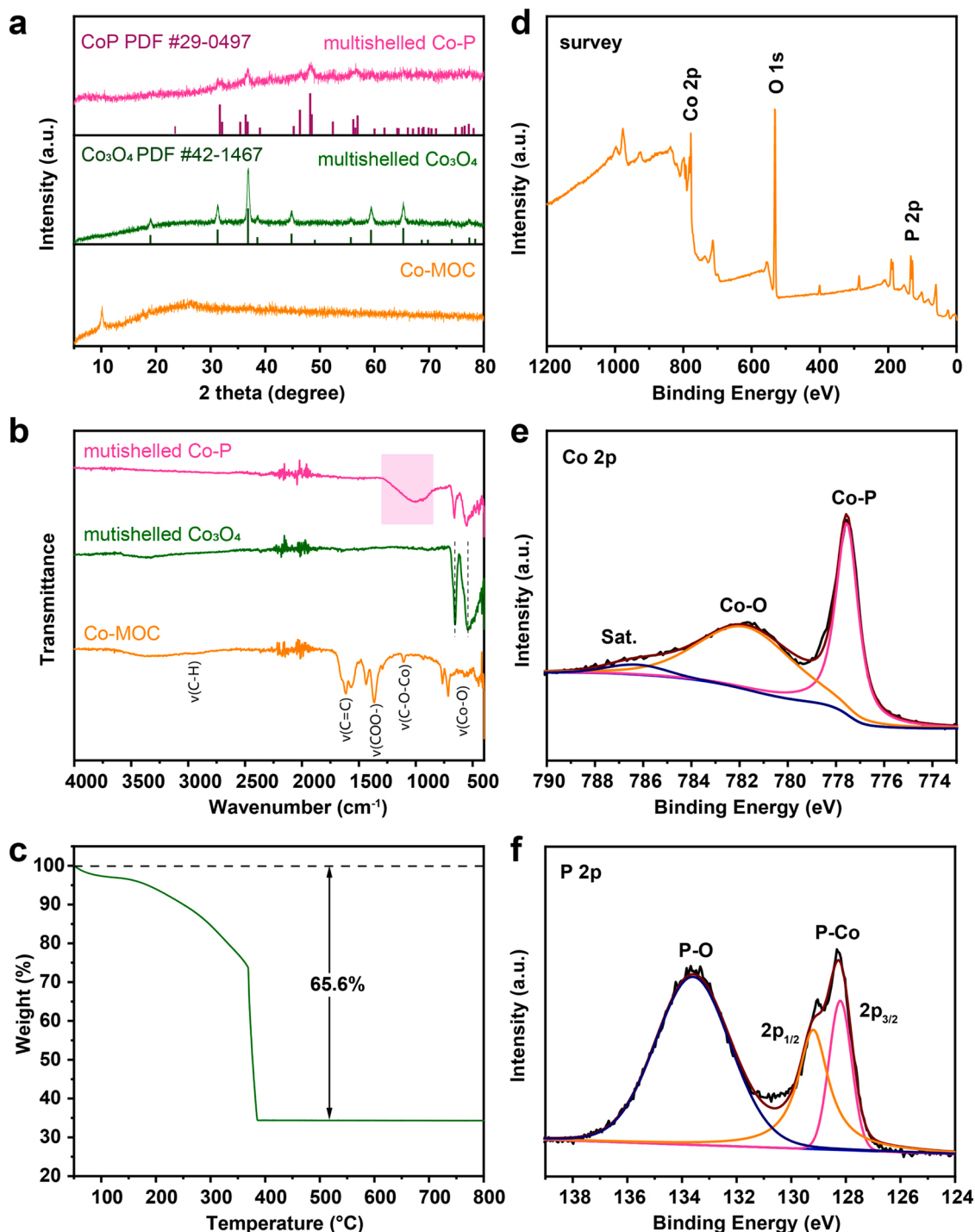


Fig. 2. (a) XRD patterns and (b) FTIR spectra of the Co-MOC precursor, multishelled Co_3O_4 and multishelled Co-P samples. (c) TGA curve of the Co-MOC precursor. XPS spectra of the multishelled Co-P: (d) survey spectrum, (e) Co 2p, and (f) P 2p.

We further carried out XPS analysis on the resultant multishelled Co-P to investigate the surface elemental composition and chemical state information. The survey spectrum (Fig. 2d) confirms the existence of the elements of Co, P, and O. In the Co 2p spectrum (Fig. 2e), the peaks at 777.6 eV are assigned to Co-P, and the peaks at 782.1 eV are associated with the oxidized Co species originated from superficial oxidation due to air contact [44,45]. For the P 2p spectrum (Fig. 2f), the peaks located at 128.2 and 129.2 eV correspond to the P-Co species, and the peak centered at 133.6 eV is attributed to the P-O species originated from unavoidable superficial oxidation [46–48]. The above XPS result further affirms the formation of cobalt phosphide species in the multishelled

Co-P.

For the purpose of better comparison, we have also constructed a series of control samples including the metallic Co with similar multishelled hollow structure (multishelled Co), CoP with a solid nanospherical morphology (solid Co-P), and common CoP without any morphology control (comm Co-P). To be specific, the multishelled Co control was obtained by the thermal reduction of multishelled Co_3O_4 under H_2 atmosphere; the solid Co-P and the comm Co-P were produced by the direct phosphidation thermal treatment of the Co-MOC precursor and cobalt nitrate salt, respectively. The detailed synthetic routes are described in Experimental Section and the related structural

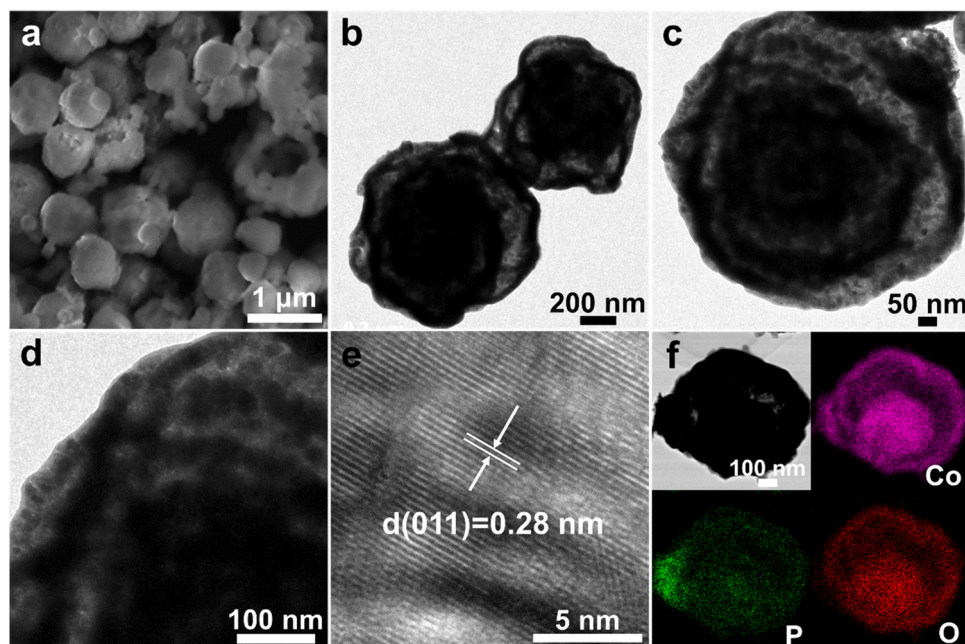


Fig. 3. (a) SEM image, (b-d) TEM images, (e) HRTEM image and (f) EDX elemental mappings of the multishelled Co-P.

characterizations are also systematically performed. As depicted in SEM and TEM images, the multishelled Co sample features multishelled hollow nanospherical structure (Fig. 4a and b), resembling the multishelled Co-P, whereas the solid Co-P sample shows solid nanospherical structure (Fig. 4c and d), and the comm Co-P sample only shows irregular aggregated particles (Fig. S3a). The XRD patterns in Fig. 4e indicate the metallic Co phase (PDF card no. 15-0806 and 05-0727) in the multishelled Co, and the orthorhombic phase of CoP (PDF card no. 29-0497) in the solid Co-P.

3.2. Catalytic dehydrogenation of AB

The H_2 evolution reaction by the hydrolytic dehydrogenation of AB with catalytic materials was assessed in AB aqueous solution at 298 K. For a thorough comparison investigation, the controls including the Co-MOC precursor, multishelled Co_3O_4 , multishelled Co, solid Co-P, and comm Co-P without morphology engineering, were also evaluated under the same testing condition. Fig. 5a displays the plots of volume of H_2 generated versus time for AB dehydrogenation catalyzed by the different samples, and the corresponding TOF values are shown in Fig. 5b. As indicated, in the absence of the catalyst, AB aqueous solution is very stable without H_2 evolution. Both the Co-MOC precursor and the

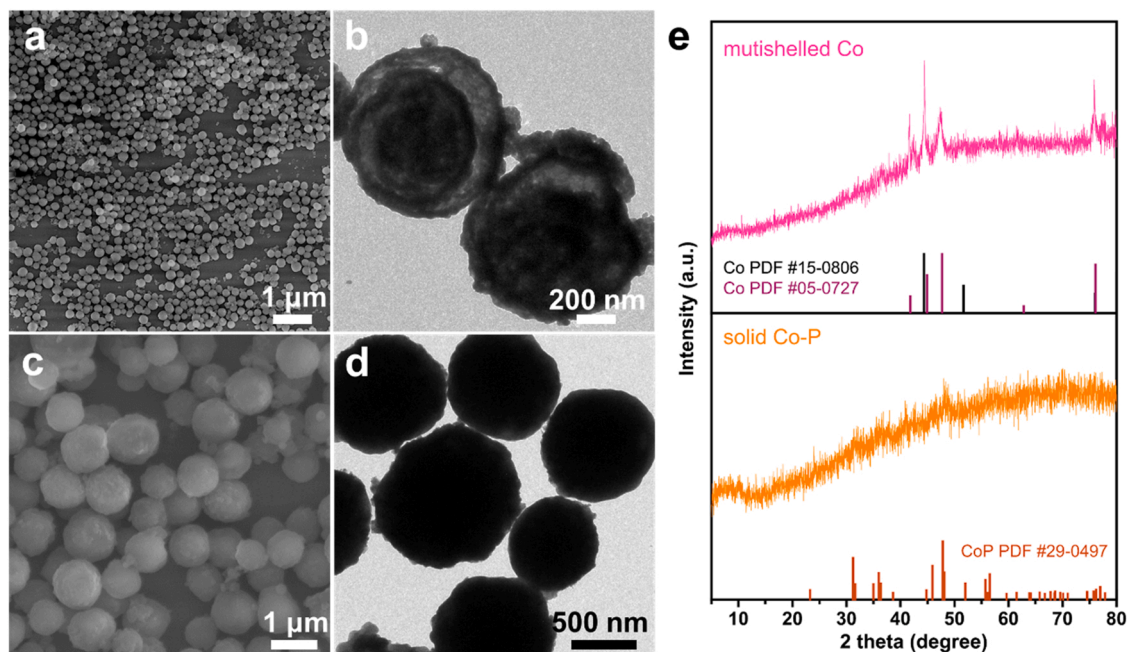


Fig. 4. (a) SEM image and (b) TEM image of the multishelled Co. (c) SEM image and (d) TEM image of the solid Co-P. (e) XRD patterns of the multishelled Co and solid Co-P samples.

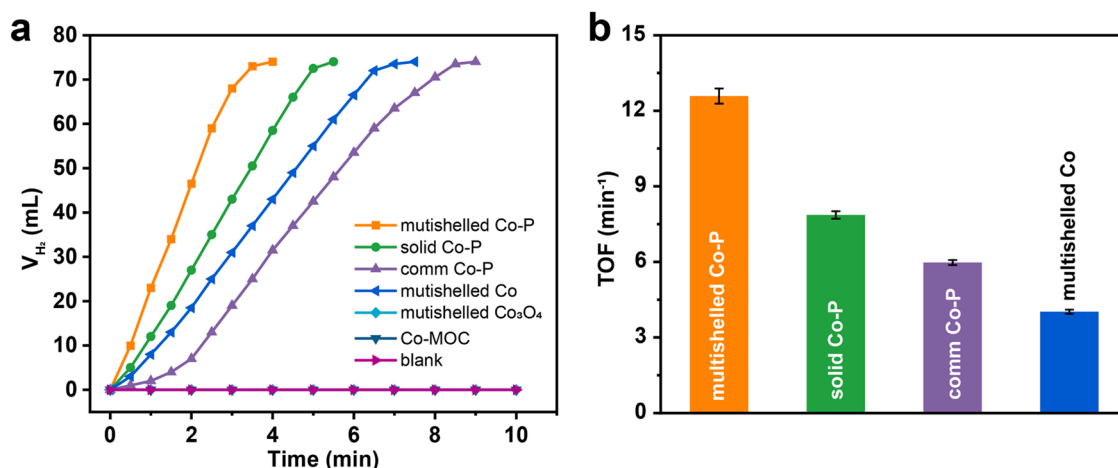


Fig. 5. (a) H₂ evolution from AB hydrolytic dehydrogenation catalyzed by different catalysts and (b) the corresponding TOF values. Reaction conditions: n(AB) = 1.0 mmol, m(catalyst) = 7.0 mg, temperature = 298 K.

multishelled Co₃O₄ present negligible catalytic behaviors for AB dehydrogenation (Fig. 5a, S4, and S5).

Impressively, upon phosphidation treatment, the as-obtained multishelled Co-P exhibits significantly enhanced catalytic activity for AB hydrolysis, i.e., only ca. 3.5 min was required to complete the reaction, affording a high TOF value of 12.6 min⁻¹. By contrast, for the other Co-P controls with varied morphologies, they are obviously inferior to the multishelled Co-P for AB dehydrogenation. Specifically, the solid nanospheres of Co-P and the comm Co-P demand ca. 5.0 and 8.5 min to finish AB decomposition with TOF values of 7.9 and 6.0 min⁻¹, respectively. The above results reveal the crucial influence of morphological and architectural engineering on the catalytic property of the material. In the case of our multishelled Co-P, the well-defined porous, multishelled, and hollow structure plays a significant role in the enhancement of catalytic activity, and the phenomenon can be interpreted from the maximized exposure of the active sites and promoted mass diffusion endowed by such nanoarchitecture. In addition, the multishelled Co shows a moderate catalytic activity with 7.0 min for complete hydrolytic reaction (TOF value = 4.0 min⁻¹), underperforming the multishelled Co-P. Considering the similar multishelled morphology of the aforementioned two samples, their contrasting catalytic activities on AB dehydrogenation disclose that CoP species possesses higher intrinsic catalytic activity in comparison with the metallic Co counterpart. The origin of the enhanced intrinsic catalytic activity of the CoP (vs. metallic Co) will be elaborated in the later part.

Additionally, the reaction kinetics of AB hydrolytic dehydrogenation catalyzed by the multishelled Co-P were studied. The effect of catalyst amount was firstly investigated. As shown in Fig. 6a, H₂ evolution rate increases sharply with the increase of catalyst dose, and the highest TOF value of 23.5 min⁻¹ can be achieved when using 14.0 mg of multishelled Co-P (Fig. 6b). Notably, such TOF value of the multishelled Co-P can favorably compete with those of the state-of-the-art catalysts reported so far (Table S1) [13,49–53]. Furthermore, AB hydrolytic dehydrogenation over multishelled Co-P was also performed with varied concentrations of AB (Fig. 6c). The corresponding logarithmic plot of H₂ evolution rate versus the concentration of AB is depicted in Fig. 6d, and the slope is calculated to be 0.12, suggesting that AB hydrolytic dehydrogenation with respect to the concentration of AB follows the zero-order kinetics when utilizing multishelled Co-P as the catalyst. The above result unveils that activation of AB is facile, that is, the rate-determining step (RDS) of the whole reaction would not involve AB activation.

Moreover, catalytic AB hydrolysis over the multishelled Co-P sample was also carried out at different reaction temperatures to study the reaction activation energy (E_a). As presented in Fig. 6e and f, H₂ releases faster with the increase of the reaction temperature, and the E_a of the

multishelled Co-P is calculated to be 38.7 kJ mol⁻¹ from the Arrhenius plot. Of note, the multishelled Co-P developed in this study, with such exceptional catalytic behavior, can rival the recent reported high-performing catalysts for AB dehydrogenation [13,14,17,52,53]. A detailed comparison can be found in Table S1.

Furthermore, the durability of the multishelled Co-P for the catalytic AB dehydrogenation was also studied. As depicted in Fig. 7a, the multishelled Co-P can be reused for up to 7 cycles without noticeable catalytic activity decay. The observed slight drop in activity could be ascribed to the partial coverage of the active sites by the continuously produced BO₂ species. Additionally, physical damage to the catalyst caused by the magnetic stirrer during reaction is probably also a reason for activity decay. The TEM image (Fig. 7b) reveals that the original multishelled morphology is largely retained. And the XRD pattern in Fig. S6 exhibits the same diffraction peaks of CoP (PDF card no. 29-0497) with the fresh one, demonstrating decent stability in crystal structure. The above results collectively manifest the robustness of the multishelled Co-P sample for catalytic AB dehydrogenation.

3.3. Fundamental understanding on the origin of enhanced catalytic performance

According to the above systematical material characterizations and performance evaluations, we could infer that the unique architecture in combination with the intrinsic electronic property of CoP species collectively contribute to the remarkably enhanced catalytic AB dehydrogenation activity of the multishelled Co-P. On the one hand, the special morphology regarding multiple porous shells and hollow structure with complicated nanoconfined interior space is advantageous for fully exposing the catalytic active sites and meanwhile speeding up the mass diffusion, thus accelerating the catalytic process. On the other hand, it is well-documented that for a transition metal compound, the intrinsic catalytic property is highly dependent on its surface electronic state, which can be tailored via the surrounding anionic structure [54–57]. In this context, we could tentatively propose that in the case of the multishelled Co-P, the introduction of P species can effectively regulate the electronic structure and local coordination environment of the Co centers, thus optimizing the adsorption/desorption processes of the reaction intermediates, thereby boosting the reaction kinetics of AB dehydrogenation. As a consequence, the resulting multishelled Co-P can possess better catalytic activity than the pure metallic Co with similar morphology.

It has been reported that initial H₂O adsorption is critical to AB dehydrogenation [11,58–60]. Herein we carried out water contact angle measurement to investigate the wettability of the multishelled Co-P,

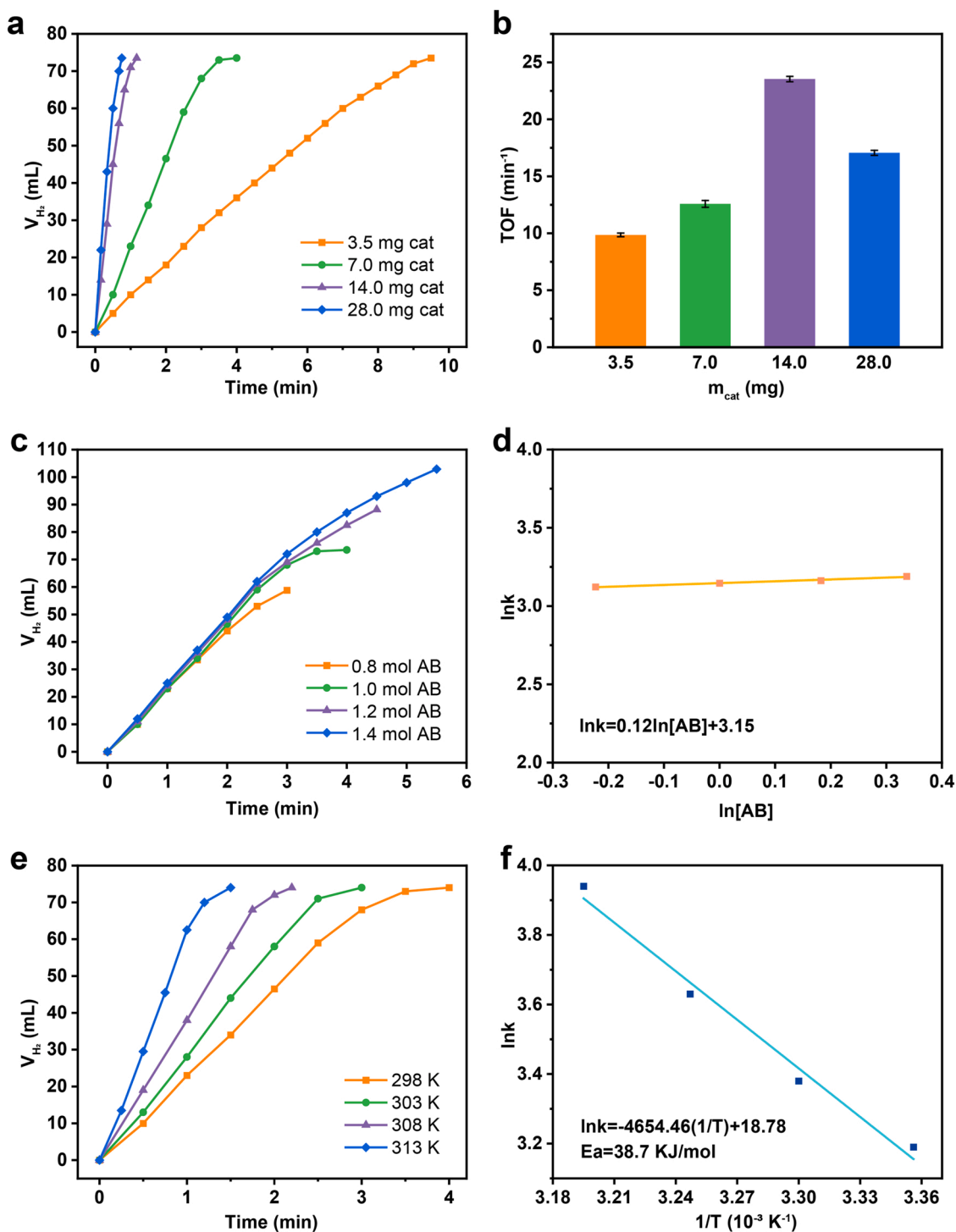


Fig. 6. (a) Relationship between H_2 evolution rate and the multishelled Co-P dose at the fixed amount of AB (1.0 mmol), and (b) the corresponding TOF values. (c) Relationship between H_2 evolution rate and AB concentration at the fixed amount of multishelled Co-P (7.0 mg), and (d) the corresponding logarithmic plot of H_2 evolution rate versus $[AB]$. (e) H_2 evolution from AB dehydrogenation catalyzed by the multishelled Co-P at different reaction temperatures in the range of 298–313 K, and (f) the corresponding Arrhenius plot.

multishelled Co, and comm Co-P. As illustrated in Fig. 8a and b, the multishelled Co-P shows an initial contact angle of 18.8° at 0 s, much smaller than that of multishelled Co (44.4°), indicating that multishelled Co-P with nonmetal P incorporation is much more hydrophilic than the multishelled Co. Additionally, the comm Co-P displays an initial contact angle of 26.7° (Fig. 8c), which is larger than that of multishelled Co-P (18.8°). It is known that surface wettability of the material is largely determined by its surface composition and morphological structure.

Based on the above knowledge, the contrasting wetting behaviors between comm Co-P and multishelled Co-P can be interpreted from their distinct morphologies, and impressively, the unique porous multishelled hollow structure can contribute to promoting hydrophilicity of the multishelled Co-P. Obviously, it can be expected that the improved hydrophilicity of multishelled Co-P would ensure smooth transportation of AB and H_2O to activate, thus contributing to the promotion of AB hydrolytic dehydrogenation.

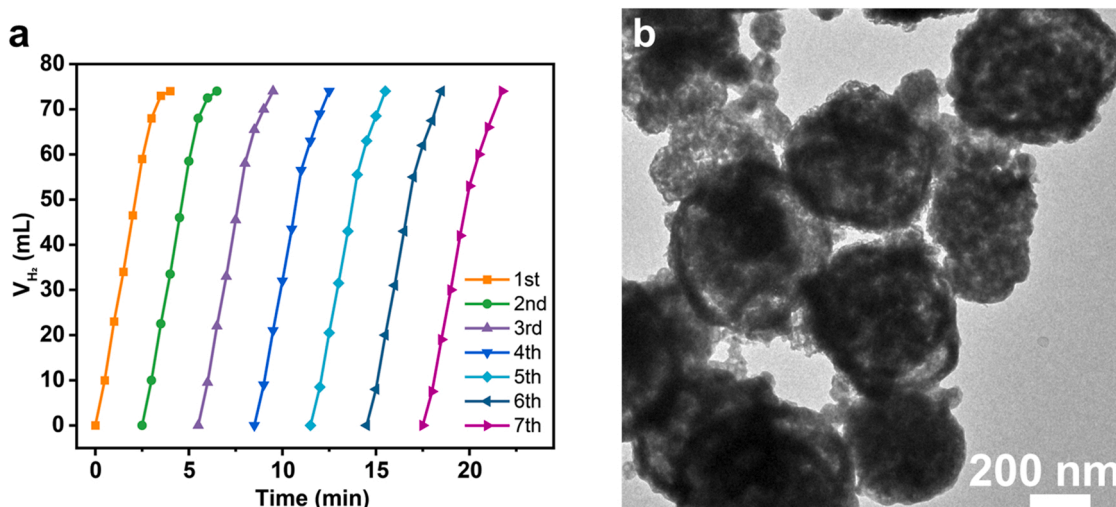


Fig. 7. (a) Stability test of the AB dehydrogenation catalyzed by the multishelled Co-P. Reaction conditions: $n(\text{AB}) = 1.0$ mmol, $m(\text{catalyst}) = 7.0$ mg, temperature = 298 K. (b) TEM image of the multishelled Co-P after the stability test.

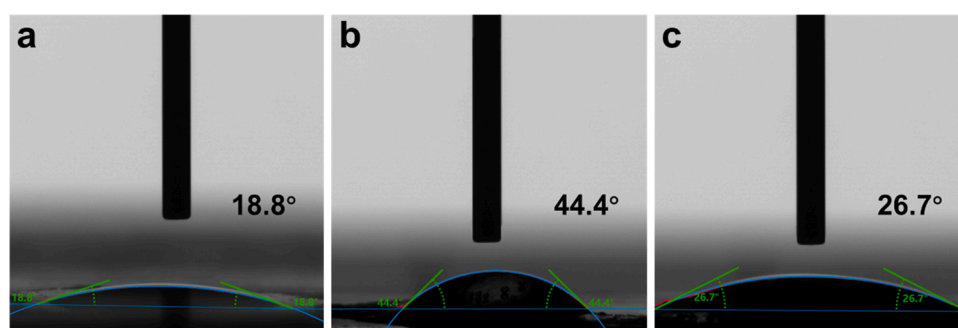


Fig. 8. Water contact angle measurements of the samples: (a) multishelled Co-P, (b) multishelled Co, and (c) comm Co-P. The photos were taken once the droplets were dropped on the surface of the samples (time = 0 s).

Further, to better illuminate the electronic modulation of the multishelled Co-P for promoted AB dehydrogenation, density functional theory (DFT) calculations were performed on CoP and metallic Co. As exhibited in Fig. 9a and b, the density of states (DOS) of the CoP differs from that of the metallic Co, demonstrating the electronic regulation of the CoP by incorporating the P species. For better illustration, the projected d-orbital DOS of the Co and CoP were shown in Fig. 9c and the d-band center positions were evaluated. As indicated, the CoP possesses higher d-band center (-1.89 eV) than the Co (-1.93 eV). According to the classical d-band theory, the position of d-band center has crucial impact on the binding energy between catalyst surface and adsorbate [61–65]. The upshift of the d-band center would give rise to stronger binding strength, and vice versa [66,67]. Based on the above knowledge, in the case of CoP, nonmetal P species incorporation could modulate the electronic structure of Co, upshifting the d-band center, thereby leading to stronger metal-adsorbate binding strength compared with pristine Co (Fig. 9d).

On another front, it has been reported that apart from H_2O adsorption step, the following H_2O cleavage is also an important step for AB dehydrogenation [13,60]. Particularly, the cleavage of H_2O to produce the adsorbed OH^* and H^* species is regarded as the rate-determining step (RDS) [7,11,22,59]. Based on the above considerations, the adsorption energy of H_2O ($E_{\text{ads}}(\text{H}_2\text{O})$) and the activation energy barrier for H_2O cleavage ($E_{\text{ac}}(\text{H}_2\text{O})$) on the samples were calculated. The computational results demonstrate that Co-P ($E_{\text{ads}}(\text{H}_2\text{O}) = -0.64$ eV) is more ready for H_2O adsorption in comparison with Co ($E_{\text{ads}}(\text{H}_2\text{O}) = -0.29$ eV) (Fig. 9e), in line with the aforementioned d-band center

trend. And Fig. 9g presents the optimized atomic structures for H_2O adsorption on Co and CoP surfaces. In addition, as illustrated the energy profile of H_2O dissociation in Fig. 9f, it can be observed that CoP possesses lower $E_{\text{ac}}(\text{H}_2\text{O})$ (0.93 eV) than that of Co (0.97 eV), suggesting that P species incorporation in CoP can boost H_2O cleavage. Taken together, the superior catalytic behavior of CoP to Co in AB dehydrogenation can be explained from its optimized electronic configuration and coordination environment by incorporating P species via electronic interaction, thus promoting H_2O adsorption together with follow-up H_2O dissociation (RDS), thereby giving rise to dramatically boosted catalytic AB dehydrogenation.

4. Conclusion

In summary, we have proposed a novel and controlled synthetic approach to construct Co-P with porous multishelled hollow structure for remarkably enhanced catalytic AB hydrolytic dehydrogenation. The multishelled Co-P can be achieved from the Co-MOC through a simple self-templating conversion followed by phosphidation treatment. Specifically, the hollow porous structure and complicated nanoconfined interior space can endow the multishelled Co-P with plentiful catalytic active sites and smooth mass diffusion, thus rendering boosted catalysis. As a consequence, the multishelled Co-P is capable of delivering a prominent catalytic AB dehydrogenation performance with a high TOF value of 23.5 min^{-1} and a low E_a of 38.7 kJ mol^{-1} at 298 K, comparable to the most active earth-abundant catalysts reported to date. Significantly, from the DFT calculations, it is unveiled that P species

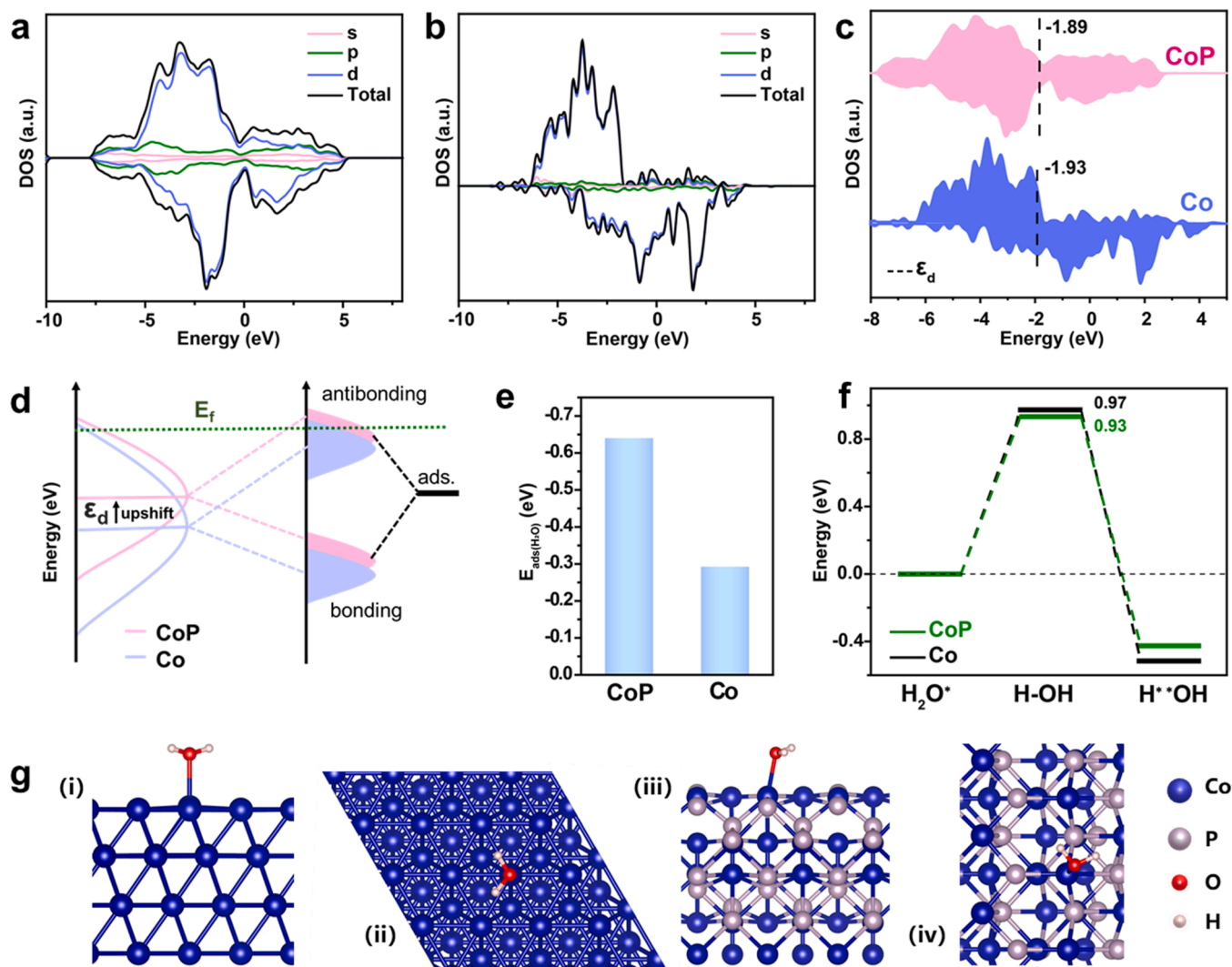


Fig. 9. Density functional theory (DFT) calculations. The density of states (DOS) of the (a) CoP, (b) Co model surfaces. (c) The calculated projected d-orbital DOS of CoP and Co. (d) Schematic illustration of the bond formation between the CoP or Co surface and the adsorbate (ads.). (e) The H₂O adsorption energy ($E_{\text{ads}}(\text{H}_2\text{O})$) and (f) the energy profiles of H₂O dissociation on CoP and Co surfaces. (g) The optimized geometrical structures for H₂O adsorption on Co model surface (i and ii) and CoP model surface (iii and iv) from the side and top view, respectively.

engineering in Co-P can favorably regulate the electronic state of the Co centers with elevated d-band center to boost H₂O adsorption and speed up H₂O dissociation (RDS), thus leading to expediting AB dehydrogenation. The work presented herein not only brings more insightful understanding of AB dehydrogenation on TMPs, but also inspires the development of other high-performing catalytic systems through elegant design over the micro-/nano-structure and electronic configuration of the material for AB dehydrogenation and beyond.

CRediT authorship contribution statement

Ping Li: Conceptualization, Project administration, Writing – review & editing, Supervision, Funding acquisition. **Yuqi Huang:** Conceptualization, Methodology, Formal analysis, Investigation, Resources, Visualization, Writing – original draft. **Qihua Huang:** Investigation, Resources, Visualization. **Ran Chen:** Resources, Methodology, Investigation, Formal analysis, Data curation, Writing – original draft. **Jixin Li:** Data curation, Validation. **Shuanghong Tian:** Supervision, Writing – review & editing.

Declaration of Competing Interest

The authors declare that they have no known competing financial interests or personal relationships that could have appeared to influence the work reported in this paper.

Acknowledgements

The research is supported by the National Natural Science Foundation of China (No. 52002412 and 22072186), the Natural Science Foundation of Guangdong Province (No. 2021A1515010575), Guangzhou Science and Technology Plan General Project (202102020862).

Appendix A. Supporting information

Supplementary data associated with this article can be found in the online version at [doi:10.1016/j.apcatb.2022.121444](https://doi.org/10.1016/j.apcatb.2022.121444).

References

- [1] J. Yang, A. Sudik, C. Wolverton, D.J. Siegel, High capacity hydrogen storage materials: attributes for automotive applications and techniques for materials

- discovery, *Chem. Soc. Rev.* 39 (2010) 656–675, <https://doi.org/10.1039/B802882F>.
- [2] C. Wang, D. Astruc, Recent developments of nanocatalyzed liquid-phase hydrogen generation, *Chem. Soc. Rev.* 50 (2021) 3437–3484, <https://doi.org/10.1039/D0CS00515K>.
 - [3] A. Staibitz, A.P.M. Robertson, I. Manners, Ammonia-borane and related compounds as dihydrogen sources, *Chem. Rev.* 110 (2010) 4079–4124, <https://doi.org/10.1021/cr100088b>.
 - [4] Q. Sun, N. Wang, R. Bai, Y. Hui, T. Zhang, D.A. Do, P. Zhang, L. Song, S. Miao, J. Yu, Synergetic effect of ultrasmall metal clusters and zeolites promoting hydrogen generation, *Adv. Sci.* 6 (2019) 1802350, <https://doi.org/10.1002/advs.201802350>.
 - [5] C. Wang, Q. Wang, F. Fu, D. Astruc, Hydrogen generation upon nanocatalyzed hydrolysis of hydrogen-rich boron derivatives: recent developments, *Acc. Chem. Res.* 53 (2020) 2483–2493, <https://doi.org/10.1021/acs.accounts.0c00525>.
 - [6] W.-W. Zhan, Q.-L. Zhu, Q. Xu, Dehydrogenation of ammonia borane by metal nanoparticle catalysts, *ACS Catal.* 6 (2016) 6892–6905, <https://doi.org/10.1021/acscatal.6b02209>.
 - [7] W. Chen, D. Li, Z. Wang, G. Qian, Z. Sui, X. Duan, X. Zhou, I. Yeboah, D. Chen, Reaction mechanism and kinetics for hydrolytic dehydrogenation of ammonia borane on a Pt/CNT catalyst, *AIChE J.* 63 (2017) 60–65, DOI:doi:10.1002/aic.15389.
 - [8] L. Wang, H. Li, W. Zhang, X. Zhao, J. Qiu, A. Li, X. Zheng, Z. Hu, R. Si, J. Zeng, Supported rhodium catalysts for ammonia–borane hydrolysis: dependence of the catalytic activity on the highest occupied state of the single rhodium atoms, *Angew. Chem. Int. Ed.* 56 (2017) 4712–4718, DOI:doi:10.1002/anie.201701089.
 - [9] C. Yüksel Alpaydin, S.K. Gülbay, C. Ozgur Colpan, A review on the catalysts used for hydrogen production from ammonia borane, *Int. J. Hydrog. Energy* 45 (2019) 3414–3434, <https://doi.org/10.1016/j.ijhydene.2019.02.181>.
 - [10] H. Liu, C.Y. Cao, P. Li, Y. Yu, W.G. Song, Core-shell structured nanospheres with mesoporous silica shell and Ni core as a stable catalyst for hydrolytic dehydrogenation of ammonia borane, *J. Energy Chem.* 23 (2014) 50–56, [https://doi.org/10.1016/s2095-4956\(14\)60117-0](https://doi.org/10.1016/s2095-4956(14)60117-0).
 - [11] Z. Li, T. He, L. Liu, W. Chen, M. Zhang, G. Wu, P. Chen, Covalent triazine framework supported non-noble metal nanoparticles with superior activity for catalytic hydrolysis of ammonia borane: from mechanistic study to catalyst design, *Chem. Sci.* 8 (2017) 781–788, <https://doi.org/10.1039/C6SC02456D>.
 - [12] L. Zhou, J. Meng, P. Li, Z. Tao, L. Mai, J. Chen, Ultrasmall cobalt nanoparticles supported on nitrogen-doped porous carbon nanowires for hydrogen evolution from ammonia borane, *Mater. Horiz.* 4 (2017) 268–273, <https://doi.org/10.1039/C6MH00534A>.
 - [13] P. Li, R. Chen, Y. Huang, W. Li, S. Zhao, S. Tian, Activating transition metal via synergistic anomalous phase and doping engineering towards enhanced dehydrogenation of ammonia borane, *Appl. Catal. B* 300 (2022), 120725, <https://doi.org/10.1016/j.apcatb.2021.120725>.
 - [14] C. Cui, Y. Liu, S. Mehdi, H. Wen, B. Zhou, J. Li, B. Li, Enhancing effect of Fe-doping on the activity of nano Ni catalyst towards hydrogen evolution from NH_3BH_3 , *Appl. Catal. B* 265 (2020), 118612, <https://doi.org/10.1016/j.apcatb.2020.118612>.
 - [15] C. Li, J. Zhou, W. Gao, J. Zhao, J. Liu, Y. Zhao, M. Wei, D.G. Evans, X. Duan, Binary Cu–Co catalysts derived from hydrotalcites with excellent activity and recyclability towards NH_3BH_3 dehydrogenation, *J. Mater. Chem. A* 1 (2013) 5370–5376, <https://doi.org/10.1039/C3TA10424A>.
 - [16] K. Feng, J. Zhong, B. Zhao, H. Zhang, L. Xu, X. Sun, S.-T. Lee, $\text{Cu}_x\text{Co}_{1-x}\text{O}$ nanoparticles on graphene oxide as a synergistic catalyst for high-efficiency hydrolysis of ammonia–borane, *Angew. Chem. Int. Ed.* 55 (2016) 11950–11954, <https://doi.org/10.1002/anie.201604021>.
 - [17] J. Liao, D. Lu, G. Diao, X. Zhang, M. Zhao, H. Li, $\text{Co}_0.8\text{Cu}_{0.2}\text{MoO}_4$ microspheres composed of nanoplatelets as a robust catalyst for the hydrolysis of ammonia borane, *ACS Sustain. Chem. Eng.* 6 (2018) 5843–5851, DOI:10.1021/acsschemeng.7b03994.
 - [18] H. Sun, J. Meng, L. Jiao, F. Cheng, J. Chen, A review of transition-metal boride/phosphide-based materials for catalytic hydrogen generation from hydrolysis of boron-hydrides, *Inorg. Chem. Front.* 5 (2018) 760–772, <https://doi.org/10.1039/C8QI00044A>.
 - [19] C.-Y. Peng, L. Kang, S. Cao, Y. Chen, Z.-S. Lin, W.-F. Fu, Nanostructured Ni_2P as a robust catalyst for the hydrolytic dehydrogenation of ammonia–borane, *Angew. Chem. Int. Ed.* 54 (2015) 15725–15729, DOI:doi:10.1002/anie.201508113.
 - [20] C.-C. Hou, Q. Li, C.-J. Wang, C.-Y. Peng, Q.-Q. Chen, H.-F. Ye, W.-F. Fu, C.-M. Che, N. López, Y. Chen, Ternary Ni–Co–P nanoparticles as noble-metal-free catalysts to boost the hydrolytic dehydrogenation of ammonia-borane, *Energy Environ. Sci.* 10 (2017) 1770–1776, <https://doi.org/10.1039/C7EE01553D>.
 - [21] X. Du, C. Yang, X. Zeng, T. Wu, Y. Zhou, P. Cai, G. Cheng, W. Luo, Amorphous NiP supported on rGO for superior hydrogen generation from hydrolysis of ammonia borane, *Int. J. Hydrog. Energy* 42 (2017) 14181–14187, <https://doi.org/10.1016/j.ijhydene.2017.04.052>.
 - [22] Y. Lin, L. Yang, H. Jiang, Y. Zhang, D. Cao, C. Wu, G. Zhang, J. Jiang, L. Song, Boosted reactivity of ammonia borane dehydrogenation over Ni/Ni₂P heterostructure, *J. Phys. Chem. Lett.* 10 (2019) 1048–1054, <https://doi.org/10.1021/acs.jpclett.9b00122>.
 - [23] Y. Shi, M. Li, Y. Yu, B. Zhang, Recent advances in nanostructured transition metal phosphides: synthesis and energy-related applications, *Energy Environ. Sci.* 13 (2020) 4564–4582, <https://doi.org/10.1039/D0EE02577A>.
 - [24] L. Yu, X.Y. Yu, X.W. Lou, The design and synthesis of hollow micro-/nanostructures: present and future trends, *Adv. Mater.* 30 (2018) 1800939, DOI:doi:10.1002/adma.201800939.
 - [25] G. Zhan, P. Li, H.C. Zeng, Architectural designs and synthetic strategies of advanced nanocatalysts, *Adv. Mater.* 30 (2018) 1802094, DOI:doi:10.1002/adma.201802094.
 - [26] H.C. Zeng, Hierarchy concepts in design and synthesis of nanocatalysts, *ChemCatChem* 12 (2020) 5303–5311, <https://doi.org/10.1002/cctc.202001003>.
 - [27] P. Li, W. Liu, J.S. Dennis, H.C. Zeng, Ultrafine alloy nanoparticles converted from 2D intercalated coordination polymers for catalytic application, *Adv. Funct. Mater.* 26 (2016) 5658–5668, <https://doi.org/10.1002/adfm.201601174>.
 - [28] Y. Wei, N. Yang, K. Huang, J. Wan, F. You, R. Yu, S. Feng, D. Wang, Steering hollow multishelled structures in photocatalysis: optimizing surface and mass transport, *Adv. Mater.* 32 (2020) 2002556, <https://doi.org/10.1002/adma.202002556>.
 - [29] D.-S. Bin, Y. Li, Y.-G. Sun, S.-Y. Duan, Y. Lu, J. Ma, A.-M. Cao, Y.-S. Hu, L.-J. Wan, Structural engineering of multishelled hollow carbon nanostructures for high-performance Na-ion battery anode, *Adv. Energy Mater.* 0 (2018) 1800855, DOI:doi:10.1002/aenm.201800855.
 - [30] J.Y. Wang, Y. Cui, D. Wang, Design of hollow nanostructures for energy storage, conversion and production, *Adv. Mater.* 31 (2019) 1801993, <https://doi.org/10.1002/adma.201801993>.
 - [31] B. Li, H.C. Zeng, Architecture and preparation of hollow catalytic devices, *Adv. Mater.* 31 (2019) 1801104, <https://doi.org/10.1002/adma.201801104>.
 - [32] W. Zhu, Z. Chen, Y. Pan, R. Dai, Y. Wu, Z. Zhuang, D. Wang, Q. Peng, C. Chen, Y. Li, Functionalization of hollow nanomaterials for catalytic applications: nanoreactor construction, *Adv. Mater.* 31 (2019) 1800426, DOI:doi:10.1002/adma.201800426.
 - [33] G. Zhan, H.C. Zeng, A synthetic protocol for preparation of binary multi-shelled hollow spheres and their enhanced oxidation application, *Chem. Mater.* 29 (2017) 10104–10112, <https://doi.org/10.1021/acs.chemmater.7b03875>.
 - [34] S. Peng, F. Gong, L. Li, D. Yu, D. Ji, T. Zhang, Z. Hu, Z. Zhang, S. Chou, Y. Du, S. Ramakrishna, Necklace-like multishelled hollow spinel oxides with oxygen vacancies for efficient water electrolysis, *J. Am. Chem. Soc.* 140 (2018) 13644–13653, <https://doi.org/10.1021/jacs.8b05134>.
 - [35] Y. Wei, J. Wan, N. Yang, Y. Yang, Y. Ma, S. Wang, J. Wang, R. Yu, L. Gu, L. Wang, L. Wang, W. Huang, D. Wang, Efficient sequential harvesting of solar light by heterogeneous hollow shells with hierarchical pores, *Natl. Sci. Rev.* 7 (2020) 1638–1646, <https://doi.org/10.1093/nsr/nwaa059>.
 - [36] P. Li, Y. Lin, S. Zhao, Y. Fu, W. Li, R. Chen, S. Tian, Defect-engineered Co_3O_4 with porous multishelled hollow architecture enables boosted advanced oxidation processes, *Appl. Catal. B* 298 (2021), 120596, <https://doi.org/10.1016/j.apcatb.2021.120596>.
 - [37] C. Livage, N. Guillou, J. Marrot, G. Ferey, Construction of two- and three-dimensional coordination polymers from cobalt trimesate, *Chem. Mater.* 13 (2001) 4387–4392, <https://doi.org/10.1021/cm011115k>.
 - [38] C.R. Wade, M. Dincă, Investigation of the synthesis, activation, and isosteric heats of CO_2 adsorption of the isostructural series of metal–organic frameworks $\text{M}_3(\text{BTC})_2$ ($\text{M} = \text{Cr}, \text{Fe}, \text{Ni}, \text{Cu}, \text{Mo}, \text{Ru}$), *Dalton Trans.* 41 (2012) 7931–7938, <https://doi.org/10.1039/C2DT30372H>.
 - [39] V. Jabbari, J.M. Veleta, M. Zarei-Chaleshtori, J. Gardea-Torresdey, D. Villagran, Green synthesis of magnetic MOF@GO and MOF@CNT hybrid nanocomposites with high adsorption capacity towards organic pollutants, *Chem. Eng. J.* 304 (2016) 774–783, <https://doi.org/10.1016/j.cej.2016.06.034>.
 - [40] Y. Li, W. Qiu, F. Qin, H. Fang, V.G. Hadjiev, D. Litvinov, J. Bao, Identification of cobalt oxides with raman scattering and fourier transform infrared spectroscopy, *J. Phys. Chem. C* 120 (2016) 4511–4516, <https://doi.org/10.1021/acs.jpcc.5b11185>.
 - [41] J. Guan, F. Mou, Z. Sun, W. Shi, Preparation of hollow spheres with controllable interior structures by heterogeneous contraction, *Chem. Commun.* 46 (2010) 6605–6607, <https://doi.org/10.1039/C0CC01044H>.
 - [42] B.Y. Guan, A. Kushima, L. Yu, S. Li, J. Li, X.W. Lou, Coordination polymers derived general synthesis of multishelled mixed metal-oxide particles for hybrid supercapacitors, *Adv. Mater.* 29 (2017) 1605902, <https://doi.org/10.1002/adma.201605902>.
 - [43] Y. Liu, H. Zou, H. Ma, J. Ko, W. Sun, K. Andrew Lin, S. Zhan, H. Wang, Highly efficient activation of peroxymonosulfate by MOF-derived CoP/CoOx heterostructured nanoparticles for the degradation of tetracycline, *Chem. Eng. J.* 430 (2022), 132816, <https://doi.org/10.1016/j.cej.2021.132816>.
 - [44] P. Li, H.C. Zeng, Promoting electrocatalytic oxygen evolution over transition-metal phosphide-based nanocomposites via architectural and electronic engineering, *ACS Appl. Mater. Interfaces* 11 (2019) 46825–46838, <https://doi.org/10.1021/acsami.9b16564>.
 - [45] Y. Men, P. Li, J. Zhou, G. Cheng, S. Chen, W. Luo, Tailoring the electronic structure of Co_2P by N doping for boosting hydrogen evolution reaction at All pH values, *ACS Catal.* 9 (2019) 3744–3752, <https://doi.org/10.1021/acscatal.9b00407>.
 - [46] P. Li, H.C. Zeng, Advanced oxygen evolution catalysis by bimetallic Ni-Fe phosphide nanoparticles encapsulated in nitrogen, phosphorus, and sulphur tri-doped porous carbon, *Chem. Commun.* 53 (2017) 6025–6028, <https://doi.org/10.1039/C7CC03005C>.
 - [47] P. Li, H.C. Zeng, Bimetallic Ni-Fe phosphide nanocomposites with controlled architecture and composition enabling highly efficient electrochemical water oxidation, *J. Mater. Chem. A* 6 (2018) 2231–2238, <https://doi.org/10.1039/C7TA10665C>.
 - [48] P. Li, W. Li, R. Chen, Y. Lin, Boosting the oxygen evolution electrocatalysis performance of iron phosphide via architectural design and electronic modulation, *ACS Sustain. Chem. Eng.* 8 (2020) 9206–9216, <https://doi.org/10.1021/acssuschemeng.0c03333>.
 - [49] Z. Xin, Z. Yufei, J. Xiaodan, Z. Yunxuan, S. Lu, W. Qing, W.G.I. N, W. Li-Zhu, T. Chen-Ho, Z. Tierui, Silica-protected ultrathin Ni_3FeN nanocatalyst for the

- efficient hydrolytic dehydrogenation of NH_3BH_3 , *Adv. Energy Mater.* 8 (2018) 1702780. DOI:doi:10.1002/aenm.201702780.
- [50] X. Yang, Q. Li, L. Li, J. Lin, X. Yang, C. Yu, Z. Liu, Y. Fang, Y. Huang, C. Tang, CuCo binary metal nanoparticles supported on boron nitride nanofibers as highly efficient catalysts for hydrogen generation from hydrolysis of ammonia borane, *J. Power Sources* 431 (2019) 135–143, <https://doi.org/10.1016/j.jpowsour.2019.05.038>.
- [51] M. Chen, R. Xiong, X. Cui, Q. Wang, X. Liu, SiO_2 -encompassed Co@N-doped porous carbon assemblies as recyclable catalysts for efficient hydrolysis of ammonia borane, *Langmuir* 35 (2019) 671–677, <https://doi.org/10.1021/acs.langmuir.8b03921>.
- [52] C. Wang, L. Li, X. Yu, Z. Lu, X. Zhang, X. Wang, X. Yang, J. Zhao, Regulation of d-band electrons to enhance the activity of Co-based non-noble bimetal catalysts for hydrolysis of ammonia borane, *ACS Sustain. Chem. Eng.* 8 (2020) 8256–8266, <https://doi.org/10.1021/acssuschemeng.0c01475>.
- [53] S. Guan, L. An, S. Ashraf, L. Zhang, B. Li, Oxygen vacancy excites Co_3O_4 nanocrystals embedded into carbon nitride for accelerated hydrogen generation, *Appl. Catal. B* 269 (2020), 118775.
- [54] H.-F. Wang, C. Tang, B.-Q. Li, Q. Zhang, A review of anion-regulated multi-anion transition metal compounds for oxygen evolution electrocatalysis, *Inorg. Chem. Front.* 5 (2018) 521–534, <https://doi.org/10.1039/C7QI00780A>.
- [55] N. Yao, P. Li, Z. Zhou, R. Meng, G. Cheng, W. Luo, Nitrogen engineering on 3D dandelion-flower-like CoS_2 for high-performance overall water splitting, *Small* 15 (2019) 1901993, <https://doi.org/10.1002/sml.201901993>.
- [56] P. Li, Y. Lin, Q. Huang, W. Li, S. Zhao, Y. Fu, F. Chu, S. Tian, Coordination environment and architecture engineering over Co_4N -based nanocomposite for accelerating advanced oxidation processes, *Appl. Catal. B* 302 (2022), 120850, <https://doi.org/10.1016/j.apcatb.2021.120850>.
- [57] R. Boppella, J. Tan, J. Yun, S.V. Manorama, J. Moon, Anion-mediated transition metal electrocatalysts for efficient water electrolysis: Recent advances and future perspectives, *Coord. Chem. Rev.* 427 (2021), 213552, <https://doi.org/10.1016/j.ccr.2020.213552>.
- [58] C. Wang, J. Tuninetti, Z. Wang, C. Zhang, R. Ciganda, L. Salmon, S. Moya, J. Ruiz, D. Astruc, Hydrolysis of ammonia-borane over Ni/ZIF-8 nanocatalyst: high efficiency, mechanism, and controlled hydrogen release, *J. Am. Chem. Soc.* 139 (2017) 11610–11615, <https://doi.org/10.1021/jacs.7b06859>.
- [59] J. Zhang, W. Chen, H. Ge, C. Chen, W. Yan, Z. Gao, J. Gan, B. Zhang, X. Duan, Y. Qin, Synergistic effects in atomic-layer-deposited PtCox/CNTs catalysts enhancing hydrolytic dehydrogenation of ammonia borane, *Appl. Catal. B* 235 (2018) 256–263, <https://doi.org/10.1016/j.apcatb.2018.04.070>.
- [60] P. Li, R. Chen, S. Zhao, W. Li, Y. Lin, Y. Yu, Architecture control and electronic structure engineering over Ni-based nitride nanocomposite for boosting ammonia borane dehydrogenation, *Appl. Catal. B* 298 (2021), 120523, <https://doi.org/10.1016/j.apcatb.2021.120523>.
- [61] B. Hammer, J.K. Nørskov, Why gold is the noblest of all the metals, *Nature* 376 (1995) 238–240, <https://doi.org/10.1038/376238a0>.
- [62] J.K. Nørskov, T. Bligaard, J. Rossmeisl, C.H. Christensen, Towards the computational design of solid catalysts, *Nat. Chem.* 1 (2009) 37–46, <https://doi.org/10.1038/nchem.121>.
- [63] A.J. Medford, A. Vojvodic, J.S. Hummelshøj, J. Voss, F. Abild-Pedersen, F. Studt, T. Bligaard, A. Nilsson, J.K. Nørskov, From the Sabatier principle to a predictive theory of transition-metal heterogeneous catalysis, *J. Catal.* 328 (2015) 36–42, <https://doi.org/10.1016/j.jcat.2014.12.033>.
- [64] X. Zhu, Q. Guo, Y. Sun, S. Chen, J.-Q. Wang, M. Wu, W. Fu, Y. Tang, X. Duan, D. Chen, Y. Wan, Optimising surface d charge of AuPd nanoalloy catalysts for enhanced catalytic activity, *Nat. Commun.* 10 (2019) 1428, <https://doi.org/10.1038/s41467-019-09421-5>.
- [65] S. Jiao, X. Fu, H. Huang, Descriptors for the evaluation of electrocatalytic reactions: d-band theory and beyond, *Adv. Funct. Mater.* (2021) 2107651, <https://doi.org/10.1002/adfm.202107651>.
- [66] C. Wei, Y. Sun, G.G. Scherer, A.C. Fisher, M. Sherburne, J.W. Ager, Z.J. Xu, Surface composition dependent ligand effect in tuning the activity of nickel-copper bimetallic electrocatalysts toward hydrogen evolution in alkaline, *J. Am. Chem. Soc.* 142 (2020) 7765–7775, <https://doi.org/10.1021/jacs.9b12005>.
- [67] H.Y.F. Sim, J.R.T. Chen, C.S.L. Koh, H.K. Lee, X. Han, G.C. Phan-Quang, J.Y. Pang, C.L. Lay, S. Pedireddy, I.Y. Phang, E.K.L. Yeow, X.Y. Ling, ZIF-induced d-band modification in a bimetallic nanocatalyst: achieving over 44% efficiency in the ambient nitrogen reduction reaction, *Angew. Chem. Int. Ed.* 59 (2020) 16997–17003, <https://doi.org/10.1002/anie.202006071>.